Sintering of 3YSZ doped with lithium via modified wet chemical method

Sheng Yuan, Kurt Hermange, Juliette Redonnet, Vincent Garnier

Sintering of 3YSZ doped with lithium via modified wet chemical method

Sheng Yuan, Kurt Hermange, Juliette Redonnet, Vincent Garnier*

Université de Lyon-INSA de Lyon, MATEIS CNRS UMR 5510, 20 Avenue Albert Einstein, F-69621 Villeurbanne Cedex, France.

*corresponding author

Abstract

Yttria-stabilised zirconia (YSZ) materials are of great interest due to their mechanical properties, chemical inertness, low thermal conductivity and high ionic conductivity. However, a high temperature is required to consolidate the YSZ, while homogeneity problems may arise. This study proposes a modified wet chemical method for commercial YSZ sintering started from a scalable colloidal solution containing yttrium and lithium in an aqueous medium. This homogeneous mixture, adjusted by pH and Li/Y content, transforms into intermediate phases that play a key role as "cement" linking YSZ particles at low sintering temperatures. The originality consists of the use of the citric acid enabling the formation of either porous or dense microstructure depending on processing conditions. A complete follow-up of the transformation of compounds throughout the process, from liquid phase to cement, is proposed and enables us to propose the consolidation mechanism that will be useful for further optimization.

Key words: wet-chemical; sintering aid; YSZ material; sol-gel; Li-dopant

I. Introduction

Yttria-stabilized zirconia (YSZ) has been wildly used in different industrial fields for its high mechanical performance and chemical inertia even at relatively high temperatures.[1][2] Specifically, for low yttria content (< 8mol%), the YSZ stays generally in the monoclinic-tetragonal phase region which is interesting for applications in biological domains or as structural components due to its good biocompatibility and high strength.[3] With high yttria content (> 8mol%), the YSZ is more stable in the tetragonal-cubic phase which is considered a good candidate for thermal barrier coatings (TBCs) and solid electrolytes in solid oxide fuel cells (SOFCs) thanks to its low heat conductivity and high ion conductivity via oxygen ions permeation.[4][5] These applications require good phase stability and suitable microstructures of YSZ components to meet their specifications. The cubic phase YSZ solid electrolyte should be fully dense to avoid the fuel/ oxygen contact that is prone to burring risk.[6] In contrast, the TBCs need a relatively high porosity for good heat insulation.[7] The orientation of the pores is another important parameter that limits the TBCs performance, for instance, a columnar structure can display a thermal conductivity twice as higher as a lamellar structure.[8]

Many synthesis methods have been explored or are under study to pursue these high-performance YSZ-based ceramics. The straightforward one involves the sintering of YSZ powder. However, this method is delicate to prepare mechanically stable materials with high porosity; it is also difficult to obtain YSZ with high density at temperatures below 1400 °C.[9] To overcome these issues, pore forming agents [10][11] and sintering aids have been used appropriately.[12][13] Other dry processes for preparing YSZ materials are Atmospheric Plasma Spraying (APS) [14] and the Electron Beam Physical Vapour Deposition (EBPVD).[15] They have been widely applied on the industry scale because of its low manufacturing cost and simplicity. Besides, various wet-chemical routes have emerged which are characterized by the nanoscale or even atomic scale homogeneity in the mixing of raw materials. Among these methods, combustion synthesis,[16] co-precipitation, [17] polymeric complexing, [18][19] and the sol-gel process [20] have been extensively investigated due to their versatility and relatively straightforward scalability. However, studies using wet chemical methods with commercial YSZ sintering aids are lacking, which would provide a more cost-effective approach. The performance optimization of so-prepared material is often accomplished with careful precursor molecule selection, composition control, and the pH adjustment in a suitable solvent. In most cases, all these experimental parameters are independently studied, which makes the control of microstructure more tedious and challenging because of the complicated parameter-parameter interactions.[21].

To solve these problems, this study proposes a modified wet chemical method to produce porous or dense YSZ materials at a relatively low temperature by adjusting simple synthesis parameters. Nitrate salt precursor was chosen due to its relatively low decomposition temperatures and highly volatile decomposition products, which minimizes residual contaminants in the final product.[22] Depending on the addition of organic groups, the thermal decomposition process can be either a brutal combustion using nitrate as an oxidant, or a gradual decomposition. To trigger these different degradation mechanisms, citric acid was used to simultaneously regulate the pH of the solution and the stoichiometry of the nitrate/organic groups. It should be emphasized that the formation of insoluble yttrium citrate causes in aqueous media distinct chemical environment. This blend transforms to solid state that plays a key role as "cement" to interconnect the YSZ particles together at lower temperature than common sintering routes. The diffusion of the cement composition into the nanoparticle or vice versa further enhances the mechanical properties in ceramic. In addition, with a sintering aid, the formation of the interphase between cement and nanoparticles must be understood to obtain the desired mechanical properties. The main advantage of this method is that cement composition can be easily adjusted by manipulating a single operational parameter: citric acid content, instead of considering pH, concentration and chelating agent separately.

The microstructure of the final composite depends strongly on the cement's physicochemical properties and the thermal process. It is also expected that the cement phase to interact with the particle enhancing the interparticle cohesion at high temperature. Therefore, Lithium dopant have been added which is widely acknowledged for the effect on the densification and grain growth in various oxide systems including

zirconia.[9][23] The mechanism is often attributed to the formation of a low temperature liquid phase that lowers the sintering's temperature and could allow the partial dissolution of the zirconia.

2. Materials and methods

2.1 Raw materials

The commercial YSZ with 3mol% of Yttrium powder, denoted 3YSZ, was supplied by Baikowski (Poisy, France), it consists of soft spray-dried granules with an average diameter of 26.4 µm. After ultrasonic treatment, the particles diameter of the deagglomerated granules was measured in deionized water at natural pH using a laser diffractometer (Malvern Instruments, Mastersizer HYDRO 2000). The specific surface area and the main particles diameter are 14 m^2/g and 150 nm respectively, according to the powder supplier. The precursor molecules were the lithium acetate dihydrate ($LiOOCCH_3 \cdot 2H_2O$) and yttrium nitrate hemihydrate ($Y(NO_3)_3 \cdot 6H_2O$), which were directly used as purchased from Sigma-Aldrich to prepare the solutions. Among them, yttrium nitrate hemihydrate was classically applied in combustion synthesis as nitrate resource.[22]

2.2 The molecule-level configuration in the mixture

Given that the Li-based and Y-based mixture will interact with 3YSZ through the surfaces of the nanoparticles during sintering, it is thus wanted that the YSZ nanoparticles would be fully covered by Li^+ and Y^{3+} cations. Moreover, the intermediate compounds are expected to have a sufficient quantity to be detectable that allows to study the chemical changes of the system.

By adding 3.46g of 3YSZ into 15mL solution, the total 3YSZ particles surface area was estimated to be 48.4 m^2. The cation radius is 76 pm for single Li^+ cation and 90 pm for Y^{3+} cation which are fairly close. The maximum number of connecting lithium ions on all the 3YSZ surface is then $2.08E^{21}$ which correspond to a concentration of 0.23mol/L for the precursors. In the same way, the maximum number of touching yttrium ions on all the 3YSZ surface is then $1.48E^{21}$ which correspond to 0.16mol/L in the 15ml solution.

Accordingly, we chose the concentration of the lithium acetate at 0.15, 0.3, and 0.6 mol/L and fixed the yttrium nitrate concentration to 0.3 mol/L to ensure the good surface coverage of the 3YSZ particles. The corresponding Li/ Y ratios were equal to 1:2, 1:1, and 2:1, respectively. For all the samples, the overall molar ratio of Y/ Zr (considering yttrium from both the sol-gel and 3YSZ particles) remained to be 1: 2.

It is important to notice that this composition was chosen to sufficiently cover the YSZ nanoparticles by Li^+ and Y^{3+} cations. The real situation in the reactive media can be much more complicated where the presence of the solvent molecule and the other species, such as the hydrate, acetate, nitrate, and citric groups, may prevent the cation from approaching the nanoparticles.

2.3 The preparation of the solution

The salts of Li and Y were dissolved in deionized water with the ratio mentioned above. These solutions were stirred for 30 minutes at room temperature. Citric acid was used to regulate the solution's pH while it played also a chelating agent role to slow down hydrolysis reaction rate.[24] Firstly, the impact of solution pH was investigated by varying its values at 1.4, 2, 3, 4, and 5. Subsequently, the influence of Li-dopant concentration on the ceramic microstructure after sintering was examined while maintaining a constant pH value of 2. The pH of 1.4 was the lowest pH attained in this study, to avoid excessive dilution by adding too much citric acid.

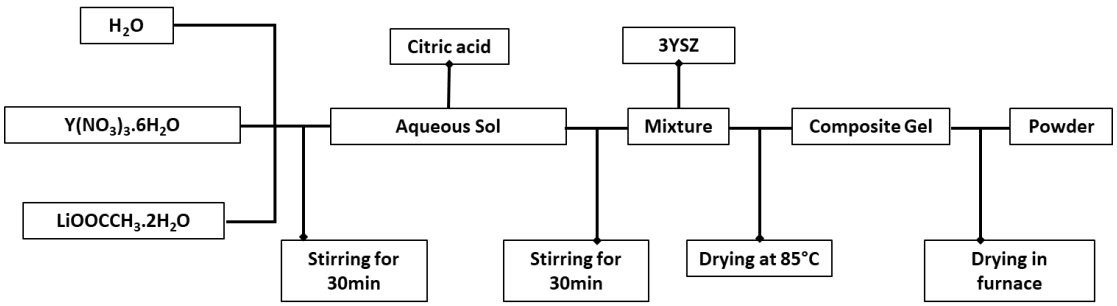

Fig. 1: the mixture preparation of the wet-chemical process.

The deagglomerated 3YSZ with a weight of 3.46g was introduced into 15ml of the previously prepared solutions. Hereafter, the samples were named depending of the different solutions' characteristics (pH and Li/Y ratio) see Table 1. The water was evaporated at 85 °C in an oil bath while the solution was carefully stirred. After 24h, a homogenous and viscous slurry could be obtained. To remove maximumly the solvent molecules, the mixtures were further dried at 85 °C in air for another 72h to form dry powder. This wet chemical route is schematically shown in Fig. 1.

Table 1: the nomenclature of the samples and the corresponding preparation conditions

Nomenclature	pH	Lithium : yttrium ratio
$Li_{1/2}Y$-pH2	2	1:2
Li_1Y-pH2	2	1:1
Li_2Y-pH1	1.4	2:1
Li_2Y-pH2	2	2:1
Li_2Y-pH3	3	2:1
Li_2Y-pH4	4	2:1
Li_2Y-pH5	5	2:1

2.4. The thermal treatment

The prepared mixtures were directly heated up to 1400 °C with a ramp of 5°C/min, maintained for 1h and then naturally cooled down to room temperature. The sample Li_2Y-pH2 that showed the most promising microstructure was furthermore heated step by step as follow to study the temperature effect on the its phases change. The calcinated powder Li_2Y-pH2 was first heated to 400 °C. Then the grey powder was grounded and compressed in a mold of 20mm diameter under 200 MPa. The prepared pellets were heated to 600 °C, 800 °C, 1000 °C, 1200 °C, and 1400 °C with a ramp of 5 °C/min.

2.5 Characterizations

All scanning electronic microscopy (SEM) images were performed with a ZEISS Supra55 equipment to study the morphology and the microstructure of the ceramics using SE detector. A low tension of 2kV was applied to prevent the charging issue on these isolated materials. Average grain diameter was determined from SEM images, considering spherical shape with the same surface area of the grains. This average diameter was measured using ImageJ software. Fourier transform infrared spectroscopy (FTIR) measurements were taken in transmission mode for the liquids and ATR mode for the powder on Thermo Scientific equipment. These results allow to probe the different chemical environment in the solutions and to track the chemical variation during calcination process. TGA-DSC analysis was carried out using Setaram's LABSYS equipment to understand the thermal degradation mechanism of the systems.This analysis was carried out under synthetic air flow and began with a stabilization step at 20 °C, then the samples were heated up to 1400 °C with a ramp of 5 °C/min in alumina crucible. The density and its uncertainty for each pellet after heat treatment was estimated by weighing and measuring their volume via the volume displacement method, using precision glassware and performing an immediate measurement to disregard water penetration into open pores. X-ray Diffraction (XRD) is a powerful nondestructive technique for characterizing material's crystallinity, which provides information about microstructure change. All XRD patterns were performed with a Bruker D8 advance instrument using a Lynx Eye high speed detector and a Cu-Kα as radiation source. The applied tension was 40 V and the current density was 20 mA while the step size was 0.05° and the scan speed was 1 sec/step. Quantification of the yttrium content in the cubic phase of zirconia was performed using the equation $\%YO1.5 = (a_{cubic} - 5.11742)/ 0.001559$ proposed by Krogstad.[25] The cubic unit cell parameter a_{cubic} was deduced from the fitted X-ray diffractogram using a pseudo-Voigt function to accurately determine the 2θ of *hkl* planes which are related to a_{cubic} according to Bragg's law.

3. Results and discussion

3.1 The state of the solutions as a function of the pH value

The pH value of the solutions, which was controlled by the amount of citric acid, played a crucial role in adjusting the equilibrium of the solutions with pre-determined cation concentrations. As a result, the solutions exhibited different states depending on their pH levels.

Without adding citric acid, the yttrium cation released from the nitrate salt attracts electrostatically the lone electron pairs from oxygen of the water molecule inducing the formation of an ordered hydration shell around the cation. This hydration product is noted $[Y(H_2O)_n]^{3+}$ and is often called an aqua cation. In $[Y(H_2O)_n]^{3+}$, the electronic attractive force is strong enough to allow formation of a steady Y-O interaction as in many cases of transition metals. Meanwhile, the electron cloud of the involved O-H bonding shifts to the oxygen atom side resulting in the dissociation of a proton into the solution. The reaction can be written as the following equation with the formation of hydroxo ions.[26]

$$[Y(H_2O)_n]^{3+} + hH_2O \leftrightarrows [Y(OH)_h(H_2O)_{n-h}]^{(3-h)+} + hH_3O^+ \quad \text{eq. 1}$$

This reaction conducts an acidic behavior (pH = 5.7) of the precursors' solution without adding citric acid.

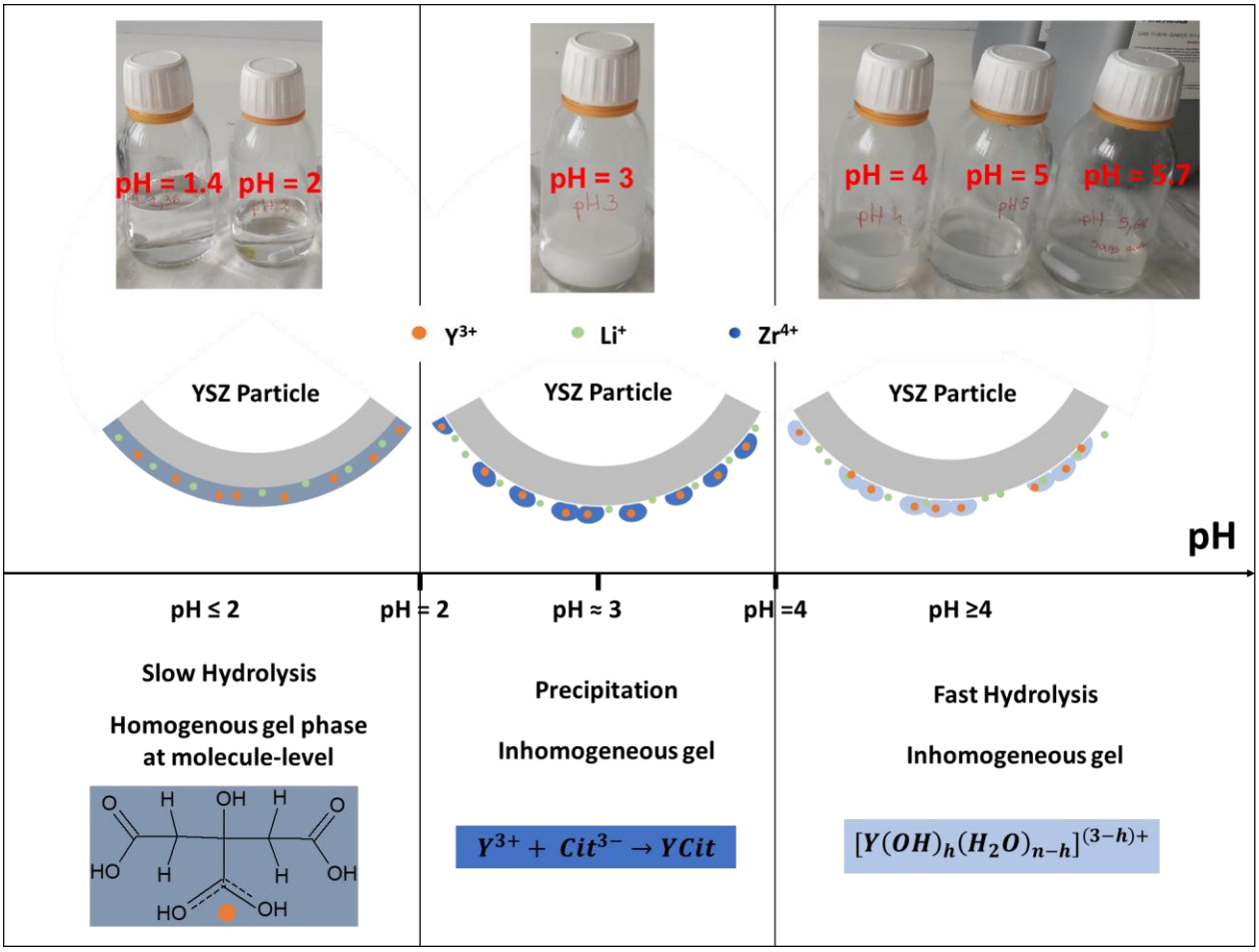

Fig. 2: the solutions variation and the illustration of the mixture system on YSZ nanoparticle surface as a function the pH value.

It can be observed that the solutions were not completely transparent but shows a little turbidity for a pH value higher than 4, see Fig. 2. Continuedly adding citric acid, a sedimentation was observed at pH = 3 while the solution suddenly became milky white. The sediment disappeared when the pH decreased to 2. The solutions with pH lower than 2 were transparent and had a relatively low viscosity which can remained stable

after 96h of storage under room temperature. During this pH variation, the molar ratio between Li-precursor and Y-precursor (1:2, 1:1, and 2:1) of different samples did not exhibit a significant effect on the solution state. The effect of citric acid on the complex's production will be carefully discussed in the section 3.2.

3.2 The chemical change of the solution characterized by FTIR

Based on the aforementioned solution observation, the phenomenon can be categorized into three distinct pH ranges. To analyze the chemical compositions at different pH values, FTIR was used and the characteristic bands of the involved groups are summarized in table 2 as reference. Fig. 3 displays the FTIR spectra obtained from solutions with various pH, while maintaining a fixed Li/Y ratio of 2:1.

Table 2: the ATR-FTIR signals of chemical groups involved

Groups	**ATR-FTIR signals wavelength (cm^{-1})**	**ref**
Acetate	1579 (antisymmetric stretching of the COO group) 1412 (symmetric stretching of the COO group), 1312 C-O stretch), 1043 (bending of theCH_3 group)	[27][28]
Nitrate	1343 (NO_3 asymmetric stretching), 825 (NO_3 symmetric stretching), 741	[29][30]
Citric acid	1710, 1250, 1075	[31][32]
Complex Citrate/ Y^{3+}	1633	[31][32]
Y-O bondings	< 700	[33]

When pH > 4, the solution is named as "sol-gel" stage. The yttrium hydroxo et aqua predominate in the solution according to the speciation graph of yttrium cation.[34] The turbidity in samples Li_2Y-pH4 and Li_2Y-pH5 was caused by the agglomeration of the nanosized colloids formed via rapid condensation (Olation and Oxolation) reactions. It should be noted that a homogeneous colloidal solution can be obtained by optimizing the parameters of the sol-gel process. However, since it is not the focus of this study, it will not be discussed in detail. At this stage, the infrared spectra exhibit well-defined Y-OH and Y-O bonding stretch bands at wavelengths below 700 cm^{-1}, as indicated in Figure 3 for the samples Li_2Y-pH4 and Li_2Y-pH5.

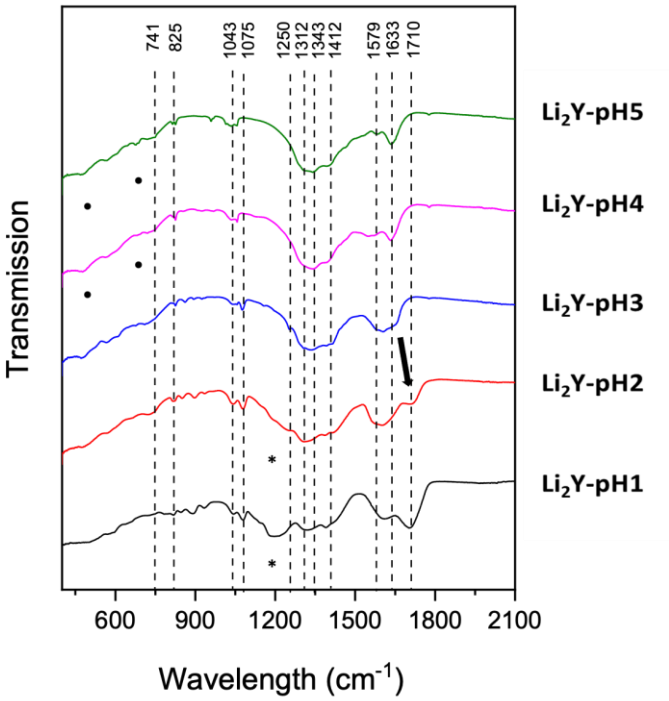

Fig. 3: FT-IR spectra recorded with the samples of different pH values while maintaining a fixed Li/Y ratio of 2:1. (•) indicate the Y-OH and Y-O bonding stretch; (*) indicate the hydrated yttrium cation; the arrow indicates the shift of the citrate to free citric acid transformation.

When pH varied from 4 to 2, the solution corresponded to a "sedimentation" stage. The transformation of the yttrium hydroxide to the yttrium citrate, denoted *YCit*, is favored under these thermodynamic conditions according the following equations:

$$Y(OH)_n^{(3-n)+} \rightarrow Y^{3+} + nOH^- \qquad \text{eq. 2}$$

$$Y^{3+} + Cit^{3-} \rightarrow YCit \qquad \text{eq. 3}$$

This transformation as well as the solubility of *YCit* in water are strongly influenced by the pH of the solution and the concentration of citrate. W. Janusz et *al.* [33]explored the logarithm of the total concentration of yttrium species as a function of pH for both the Y $(OH)_3$/water and yttrium citrate/water systems. In general, increasing citrate ion concentration shifts the boundary between the stability region of yttrium citrate and that of yttrium hydroxide towards higher pH values [35,36] Furthermore, a higher concentration of citrate ions results in increased solubility of yttrium citrate in aqueous solution. With our specific conditions, a significant amount of precipitation can be observed in sample Li_2Y-pH3 indicating the formation of insoluble *YCit*. The bonding of the Y^{3+} cation and citrate is characterized by C=O stretching vibration band at 1658 - 1604 cm^{-1} region which can be observed in the curve obtained with the sample Li_2Y-pH3, see Fig. 3.[31,32]

When pH < 2, the solution attained a "monodisperse" stage, the yttrium cation is chelated with the citrate groups forming a soluble complex due to the increasing citrate quantity. Their FTIR curves show the characteristic band of the metal aqua cation placed in the 1238 – 1176 cm^{-1} region (marked by * in Fig. 3) that can not be observed for in the FT-IR curves of the other solutions. Besides, the C=O stretching vibration band shift from 1658 - 1604 cm^{-1} to 1750 - 1710 cm^{-1} region (indicated by the arrow in Fig. 3) indicating to the transformation of the citrate anion (Cit^{3-}) combined with the Y^{3+} to a free citrate acid.[31] As a result, the solution of Li_2Y-pH1 and Li_2Y-pH2 became totally transparent.

By adjusting the citric acid content, it is possible to shift the "cursor" between the different chemical stages. On the sol-gel stage, the 3YSZ particle was mainly surrounded by yttrium hydroxide nano-colloids, while for the sedimentation stage, it is surrounded by yttrium citrate precipitates. In the monodisperse stage,

a soluble complex is formed. Besides, the nitrate and acetate anion also react with the $[Y(H_2O)_n]^{3+}$ cation by forming the metal-anion complexes in the aqueous solution:[37]

$$[Y(H_2O)_n]^{3+} + NO_3{}^- \rightarrow [Y(NO_3)(H_2O)_{n-1}]^{2+} + H_2O \quad \text{eq. 4}$$

$$[Y(H_2O)_n]^{3+} + C_2H_3O_2{}^- \rightarrow [Y(C_2H_3O_2)(H_2O)_{n-1}]^{2+} + H_2O \quad \text{eq. 5}$$

These reactions slow down the hydrolysis and condensation velocity.

3.3 The thermogravimetric analysis

The different composition effect furtherly the compounds degradation mechanism. Fig. 4 shows the TGA/DSC curves of the Li_2Y-pH2, Li_2Y-pH3, and Li_2Y-pH4 samples. The results obtained from Li_2Y-pH1 and Li_2Y-pH5, which are not presented here, are quite similar to the results of Li_2Y-pH2 and Li_2Y-pH4, respectively. Hereafter, this study will focus on these more representative samples Li_2Y-pH2, Li_2Y-pH3, and Li_2Y-pH4. At the end of the thermal treatment at 1400 °C, all samples lost ~20% - 22% of the overall weight. The first weight loss for all samples from 100 °C to 150 °C is attributed to the evaporation of the residual free water molecules. This process induced an endothermic peak centered at around 130°C.

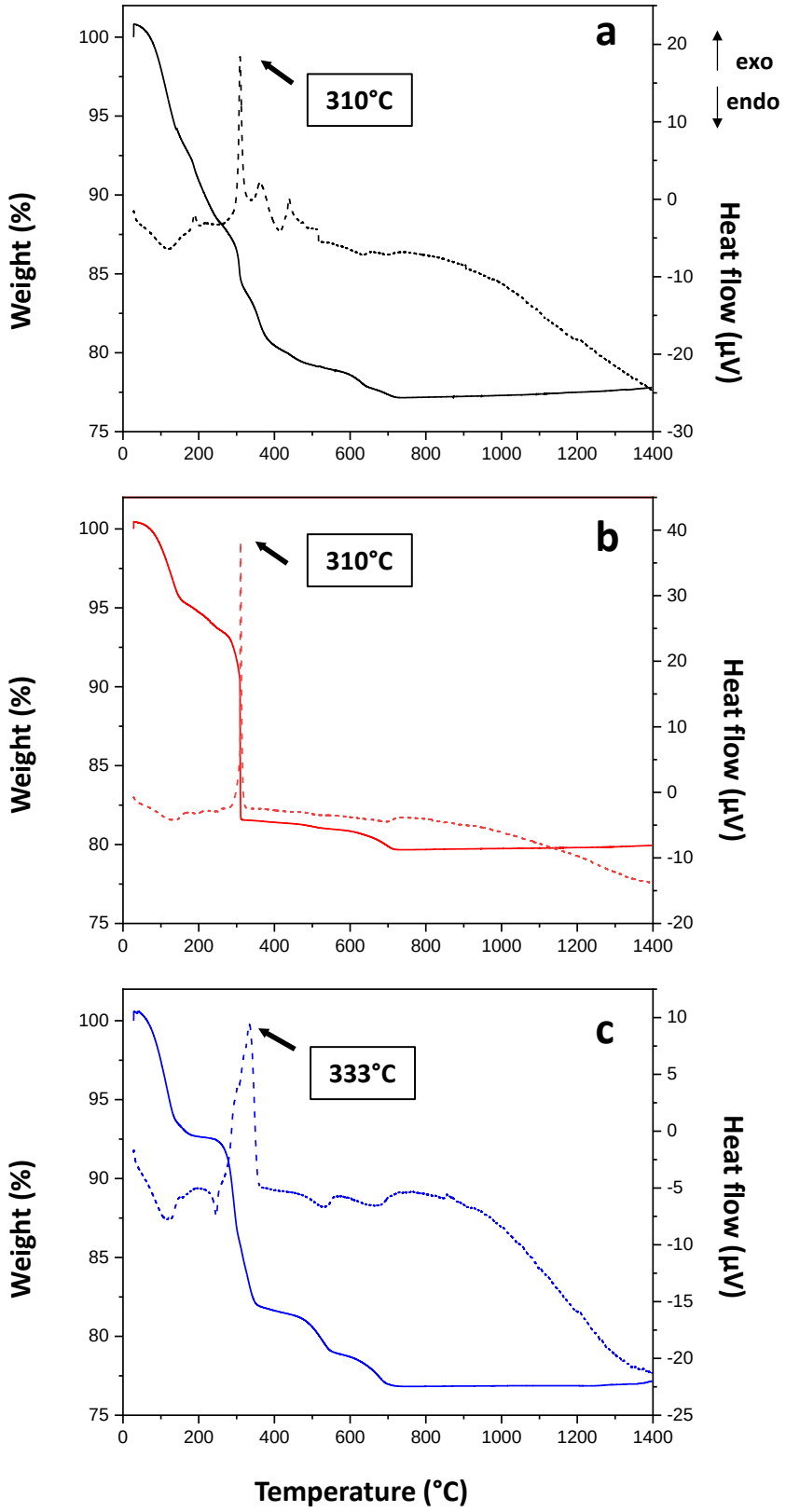

Fig. 4: the TGA-DSC curves recorded with a): Li_2Y-pH2, b): Li_2Y-pH3 and c): Li_2Y-pH4. The solid lines indicate the variation of the weight (%) and the dash lines represent the trend of the heat flow (µV).

Between 250 °C and 700 °C, main exothermic reactions took place which corresponds to the thermal degradation of the citrate, acetate, and nitrate groups.[38] [39] For Li_2Y-pH3, see Fig. 4b, there is one main narrow peak from the DSC curve accompanied by a sharp weight loss at 310 °C. This phenomenon is typically associated with a rapid redox reaction (combustion) that uses nitrate as oxidant and other organic groups (citrate and acetate) as fuel releasing different gas molecules.[40,41] A mild ignite temperature (200-300 °C), depending on the metal counterion and additives, is required to trigger this reaction. In the case of Li_2Y-pH3, the combustion was almost completed since no other significant peaks at higher temperatures were observed.

In the case of Li_2Y-pH4, Fig. 4c shows a noticeable broadening of the exothermic peak accompanied with a gradual weight loss around 333 °C compared to Li_2Y-pH3. These differences suggest that the combustion process took place with a slower velocity in Li_2Y-pH4. Indeed, the velocity of the combustion depends strongly on the nitrate/fuel ratio and the geometry of the carrier. It has been reported that the combustion (eq. 6) occurs in a bulk system while the slow decomposition (eq. 7) takes place mainly in a thin film, as shown as below: [26]

$$aM(NO_3)_{2z} + \text{organic fuel} \rightarrow aMO_z + bCO_2 + cN_2 + dH_2O \qquad \text{eq. 6}$$

$$4M(NO_3)_{2z} \rightarrow 4MO_z + 8zxNO_x + (10z-4zx)O_2 \qquad \text{eq. 7}$$

The slow progression of combustion was most likely attributed to the presence of the Yttrium hydroxide agglomeration, which leads to a discontinuity in the distribution of nitrate and fuels. As a result, a higher ignition temperature and a faster ramp are necessary for the combustion to propagate effectively.

Unlikely, the Li_2Y-pH2 curve (see Fig. 4a) displays some other exothermic peaks placed at 360 °C and 440 °C apart from the one at 310 °C. These peaks correspond to the degradation of the residual citrate and/ or acetate because an excess of citrate had been added into the solution comparing with Li_2Y-pH3.[42][43]

When the temperature became higher than 700 °C, no more evident endothermic or exothermic peaks can be observed indicating that the degradation of all the organic parts was completed. The heat flow decreases at temperatures above 800 °C generating changes in the slope of the curves. This behavior is most likely caused by phase transitions that will be discussed below.[44]

3.4 The microstructure in the calcinated powders

The SEM was used to probe the morphology and the microstructure of the raw and treated materials through calcination. Fig. 5a and b shows the SEM image of the as received raw 3YSZ powder before and after deagglomeration as reference. The granulometry analysis of the deagglomerated powder, see Fig. 5b, reveals a main peak placed at 150 - 220 nm, with some residual clusters remaining, leading to a weaker secondary peak at 1 µm. In Fig. 5c the pure 3YSZ nanoparticles heated at 1400 °C displays almost unchanged shape and size compared to the raw powder.

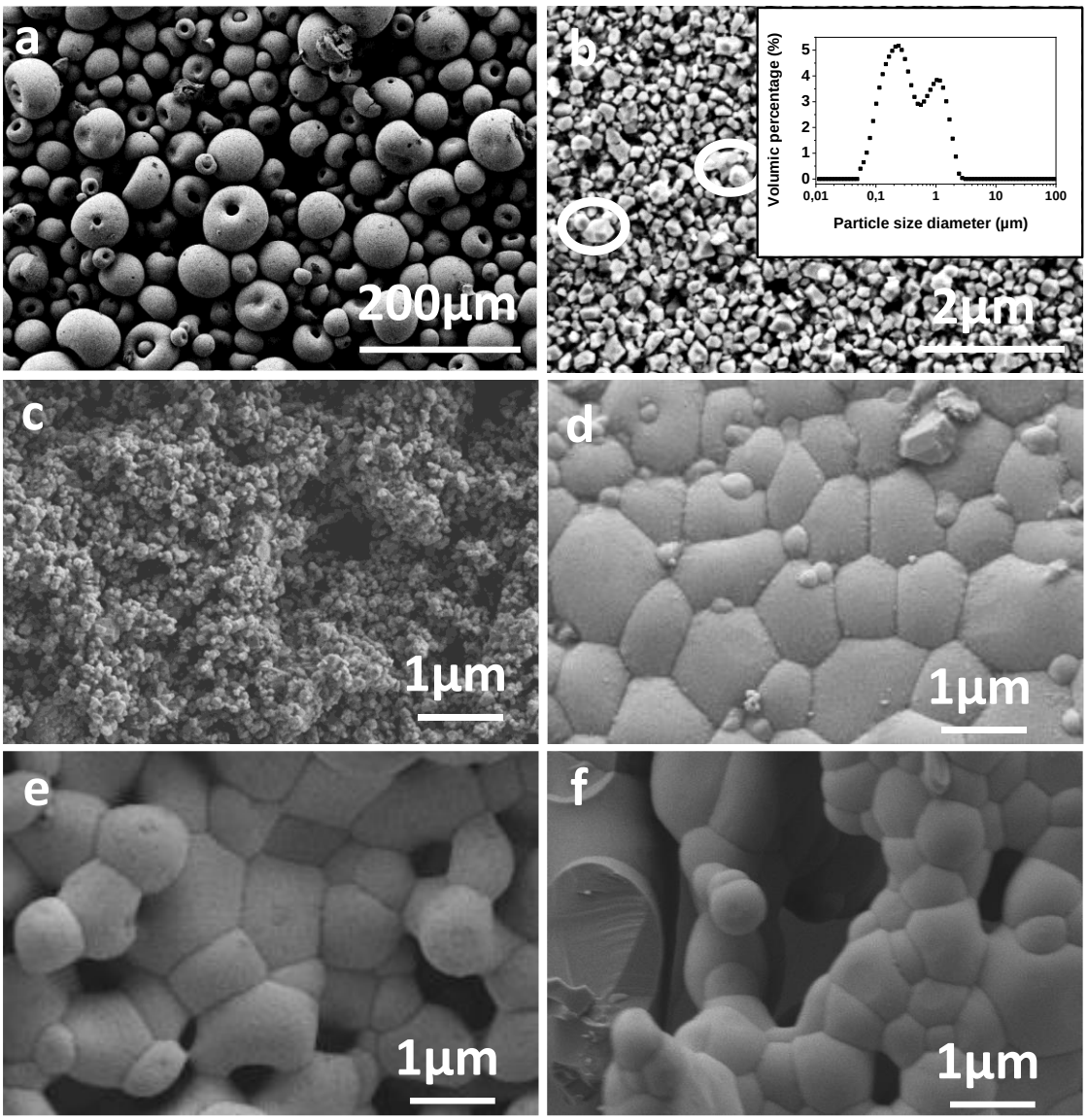

Fig. 5: the SEM image of: a) the raw 3YSZ granules powder, b) the deagglomerated powder and inset the size distribution of deagglomerated 3YSZ powder, c) the pure 3YSZ, d) Li_2Y-pH2 powder, e) Li_2Y-pH3 powder, f) Li_2Y-pH4 powder. From c) to f), the samples were sintered at 1400 °C.

3.4.1 The influence of the pH

The SEM images shown in Fig. 5d-f illustrate the powder morphology obtained with Li_2Y-pH2, Li_2Y-pH3, and Li_2Y-pH4 samples sintered at 1400 °C which have significantly bigger grain size compared with pure 3YSZ. In the case of Li_2Y-pH2, the average grain diameter and its standard deviation value are estimated, from the image analysis, of 1.1 $\pm$ 0.6 µm while the size distribution is rather broadening since submicron grain can be observed. The Li_2Y-pH3, and Li_2Y-pH4 samples average grain diameters reach 1.5 $\pm$ 0.3 µm and 1.2 $\pm$ 0.4 µm, respectively. Among these images, Li_2Y-pH2 exhibits a dense structure, while Li_2Y-pH3 displays a porous structure. This variation can be attributed to the changes in the surrounded cement phase, as discussed above. In Li_2Y-pH2, the homogenous solution and gradual degradation process contribute to the formation of a dense structure. Conversely, sedimentation and rapid combustion underwent by Li_2Y-pH3 lead to the formation of pores within the ceramic material. For pH values above 4, both Li_2Y-pH4 and Li_2Y-pH5 exhibit a duplex microstructure. This lack of homogeneity is attributed to the agglomeration of yttrium oxide, making it more

difficult to integrate into the YSZ nanoparticles cluster in aqueous media. The sol-gel stage derived product requires a further optimization to gain homogeneity which will not be discussed in this study.

The Li_2Y-pH2 and Li_2Y-pH3 samples exhibit promising potential for different applications, whether as highly dense materials or porous materials. For applications such as SOFC that require a dense structure, maintaining a pH of up to 2 is reasonable. On the other hand, if a porous structure is desired (thermal barrier material), Li_2Y-pH3 appears to be a suitable candidate. In this study, the discussion will be limited to the pH of 2 in order to investigate the effects of Li dopant on the final product. Moreover, the microstructure from dense to pores can also be tuned by the sintering conditions to meet specific applications.

3.4.2 The influence of the Li dopant quantity

With a low Li dopant quantity, some bare 3YSZ particles, as indicated by red arrows in Fig .6a, are still visible in $Li_{1/2}Y$-pH2. Fig.6a and b shows both rather porous structure for $Li_{1/2}Y$-pH2 and Li_1Y-pH2, whereas a higher Li dopant quantity in Li_2Y-pH2 leads to a significantly enhanced densification (see Fig. 6c). This microstructure variation trend emphasizes the effect of Li dopant on densification of 3YSZ. Fig. 6d shows a low-magnitude image illustrating the good homogeneity over a large observation area of Li_2Y-pH2.

The addition of lithium affects the overall system microstructure in two ways. Firstly, it increases the number of acetate groups in the mixture which reduce the thermal degradation velocity due to its higher decomposition temperature compared the nitrate. Secondly, the densification effect of lithium is dependent on its quantity. A critical amount of lithium is required to form the intermediate Li-Y-O and Li-Zr-O related eutectic liquid phases according to elsewhere report.[45] In the case of Li_2Y-pH2, the molar ratio of Li : Y : Zr reached 2 : 1 : 2, which is enough for the formation of the stoichiometric compound $LiYO_2$. Additionally, the remaining lithium seems sufficiently interact the YSZ nanoparticle surface.

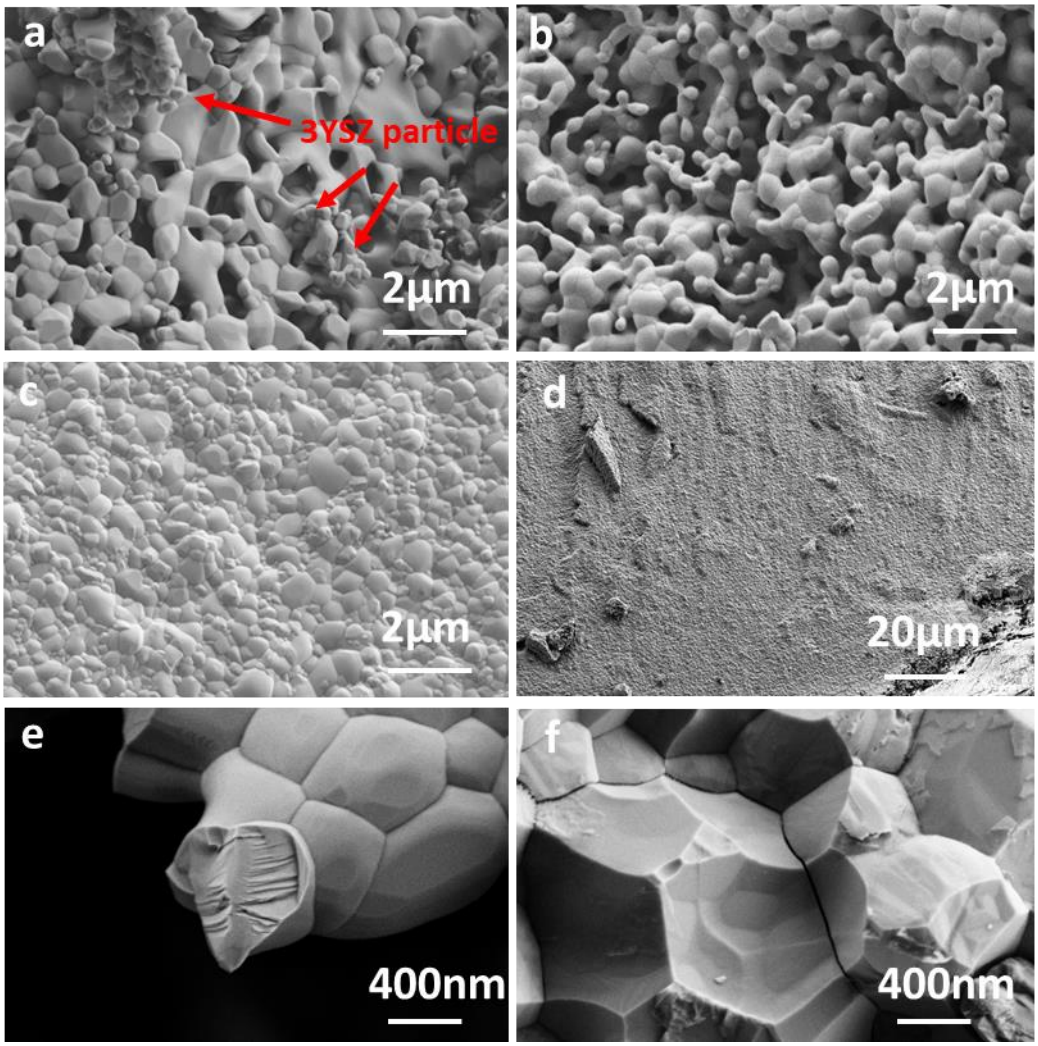

Fig. 6 the SEM image obtained with a) the $Li_{1/2}Y$-pH2 powder (red arrows indicate bare 3YSZ particles); b) the Li_1Y-pH2 powder; c) and d) Li_2Y-pH2 powder with different magnification; e) the fracture microstructure of a pure cement with a Li/Y ratio equaling to 2; f) Fracture surface of Li_2Y-pH2 microstructure.

Fig. 6f shows a fracture surface microstructure obtained with Li_2Y-pH2 which is different compared with pure cement phase (Fig.6e). The bigger grain size compared with the initial nanoparticle is due to the grain coarsening during sintering between 3YSZ and the cement phase. However, submicrometric grains remained in this polycrystalline microstructure. Furthermore, the former 3YSZ may in fact not have been coated but have disappeared, because of their transformation and growth from tetragonal to cubic phase with the yttrium brings by the cement.

3.5 The high-temperature behavior

For the following part, the sample Li_2Y-pH2 was selected to probe the high-temperature reaction and the phase transitions mechanism. The samples were first heated to 400 °C to remove maximally the organic groups according to the TGA curves, after that a grey powder was obtained. The degradation of the organics had not been fully completed yet according to the thermogravimetric plot (Fig. 4), around 92% of total weight loss underwent during this pretreatment. Moreover, the physicochemical analyses in section 3.6, specifically XRD and FTIR characterizations, exhibit similar results for the samples synthesized at both 400 °C and 600 °C. Noticeable changes only appeared at higher temperatures, thus it is reasonable to expect that no significant

chemical reactions or element diffusion took place between the cement and the Yttria-Stabilized Zirconia (YSZ) nanoparticles at 400 °C during the powder preparation process.

The pretreated powder was introduced into a mold to elaborate the pellets of 20mm diameter under 200MPa uniaxial pressure. Then during higher temperature calcination, the pellet became white at 800 °C for 1h meaning that the decarburization process was completed which is in good consistency with the thermogravimetric analysis. Then, significant shrinkage was observed from 1000 °C to 1200 °C where the sample shrunk by 30% of its volume while the density of the pellet increased from 3.6 to 4.9 g/cm^3. The trend was slightly slowed down from 1200 °C to 1400 °C where a density of 5.9 g/cm^3 at 1400 °C can be observed, as shown in Fig. 7.

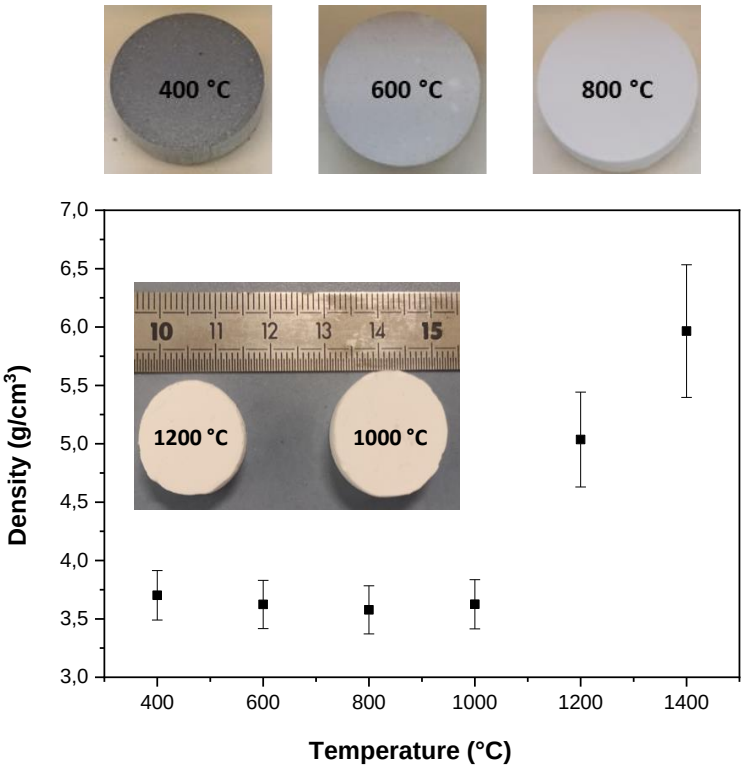

Fig. 7: the density of the pellets as function of calcination temperature

Fig. 8 show the fracture microstructure of the pellets heated for one hour at different temperature from 400 °C to 1400 °C. At low temperatures (400 – 600 °C), the 3YSZ nanoparticles were recovered by the "fungus-like" product that can no more be observed at a temperature of 800 °C. The particles are rounded and merged with the adjacent particles at 1000 °C. Meanwhile no obvious grain coarsening can be observed until this temperature. However, an important grain coarsening accompanied by a densification was observed for the sample heated at 1200 °C while the grain diameter attains 1.9 ± 0.3 µm. This dramatic variation explains the pellet volume shrinkage from 1000 °C to 1200 °C. The microstructure variation from 1200 °C to 1400 °C is not significant.

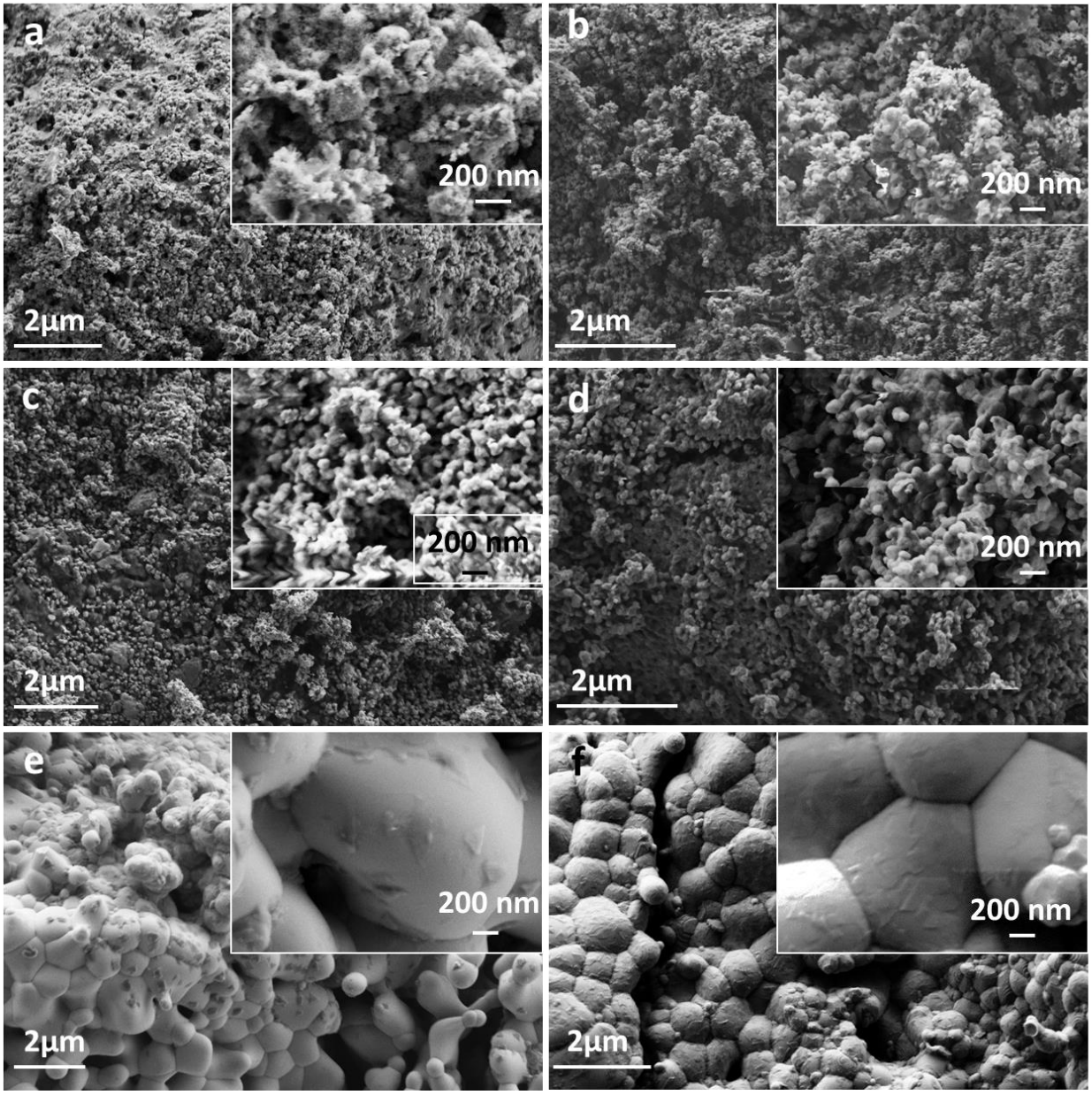

Fig. 8: SEM (2kV) images of the fracture microstructure as a function of the sintering temperature (a) 400 °C, (b) 600 °C, (c) 800 °C, (d) 1000 °C, (e) 1200 °C, (f) 1400 °C.

3.6 Densification mechanism followed by phases evolution

Fig. 9 displays the XRD patterns obtained with the pellets as a function of the sintering temperature. The diffractograms obtained with the pellets heated at 400 °C, 600 °C, and 800 °C correspond to a mixture of the tetragonal (the most intensive peak at 30°, JPCDS: 01-078-1808) and monoclinic (the most intensive peak at 28.2° and the second intensive peak at 31.5°, JPCDS: 01-083-0940) phases of 3YSZ nanoparticles. It is worth noting that the X-ray diffraction (XRD) pattern obtained from the pure 3YSZ powder exhibits identical features to those observed in the pellet heated at 400 °C and 600 °C. This similarity arises from the amorphous nature of the cement phase, and the phase transition of zirconia has not occurred under these conditions yet.

As the temperature increases, the monoclinic phase experiences a decrease in signal intensity, indicating its transition to the more stable tetragonal phase. Additionally, the tetragonal to cubic transition takes place between 800 °C and 1000 °C, which is evident by the gradual merging of the tetragonal doublet to

form a singular peak at approximately 2θ = 60°. Though residual monoclinic and tetragonal phases remain observable up to 1200 °C, only the cubic phase is present at 1400 °C. The yttrium content quantified in the cubic phase (for 1200 °C and 1400 °C) is between 10 and 12mol% Y_2O_3, calculated using the equation proposed by Krogstad [25] and the cubic unit cell parameter deduced from the X-ray diffractograms.

Regarding the cement phase, the peak labelled and located at 29.2° (JPCDS: 00-043-1036) belongs to cubic yttria indicating a local crystallization of this phase. The intensity of this peak slightly increased from 400 °C to 600 °C and became a shoulder of the tetragonal + cubic signal (2θ = 30.3°) at 1000 °C which is a result of the diffusion of yttria into the zirconia lattice. The influence of the yttria diffusion infers the zirconia lattice leading to a peak shift to a lower 2θ value (see Fig. 9b)

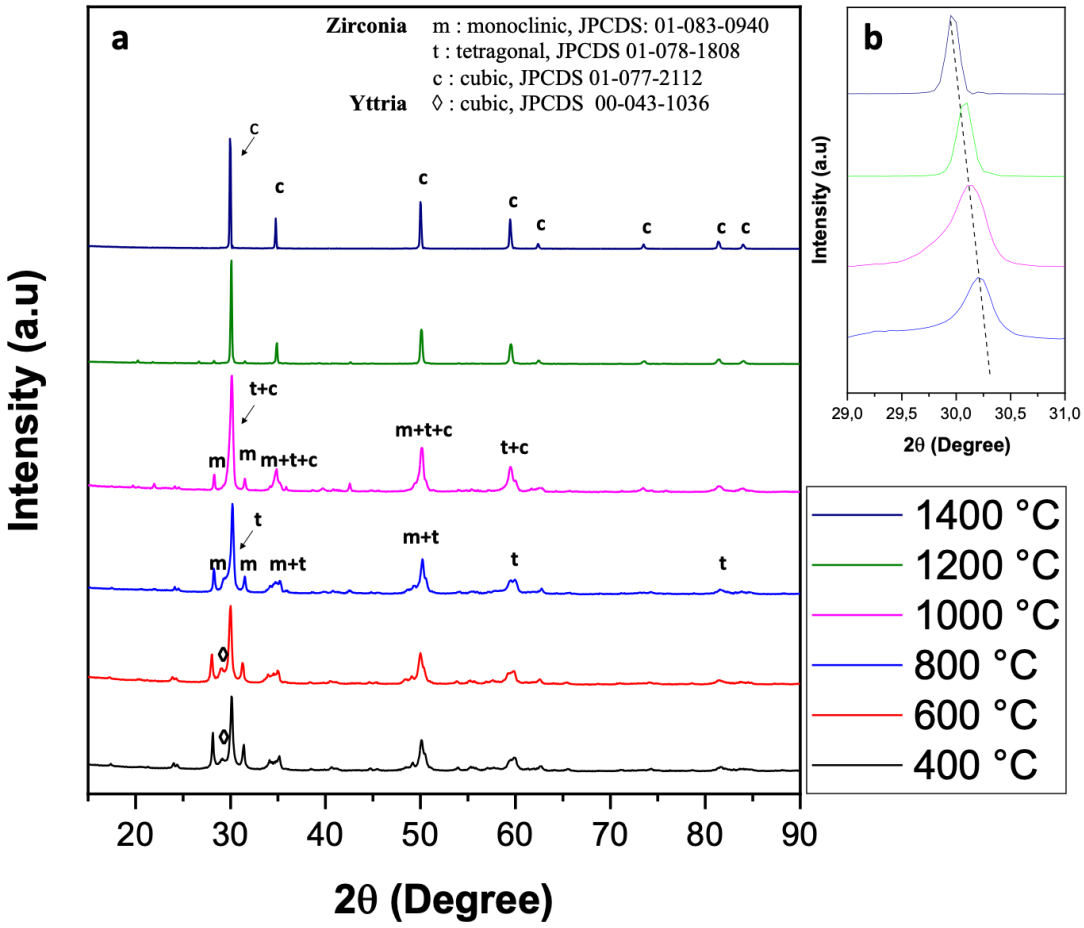

Fig. 9: a) XRD pattern of the pellets as a function of the sintering temperature; b) the peak at 30.3° shifts to a lower value from 800 °C to 1400 °C. ◊ indicates the most intensive peak of cubic yttria.

Several reactions can occur on the 3YSZ nanoparticle surface. Fig.10 shows the zoomed XRD pattern of Fig. 9 from where two additional peaks at 21.9° and 42.6° can be observed at 800 °C, which could be ascribed to the formation of a metastable tetragonal Li_2ZrO_3 compound (JCPDS:00-20-0647) via a reaction between lithium oxide from the cement phase and 3YSZ phase. At 1000 °C, this tetragonal Li_2ZrO_3 phase began to convert to monoclinic crystalline Li_2ZrO_3 (JCPDS: 01-076-1150) which is consistent elsewhere reported result.[46] At a sintering temperature of 1400 °C, the Li_2ZrO_3 peaks disappeared entirely due to its thermal degradation.

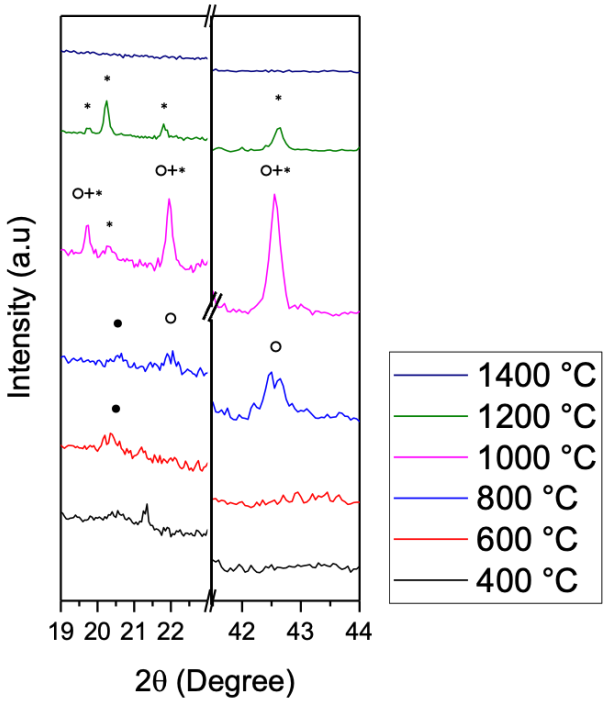

Fig. 10: XRD patterns in which the (•) represents Y_2O_3, (○) represents tetragonal Li_2ZrO_3, (*) represents monoclinic Li_2ZrO_3

Other stoichiometric compounds, $Li_6Zr_2O_7$ and Li_8ZrO_6, can also be formed, as shown by the following equations:

$3Li_2O + 2ZrO_2 \rightarrow Li_6Zr_2O_7$ eq.8

$4Li_2O + ZrO_2 \rightarrow Li_8ZrO_6$ eq.9

Limited by their small quantity and low thermal stability, these products were difficult to be directly observed after a relatively long heating process.[9] Furthermore, the most intensive diffraction peak of Li_8ZrO_6 (JCPDS: 00-026-0867) is located at 19.6° that is mainly overlapped with the signal of Li_2ZrO_3, making it difficult to verify its presence. However, it is important to notice that these stoichiometric compounds ($Li_6Zr_2O_7$, Li_8ZrO_6) allow the formation of a liquid phase due to an eutectic degradation as low as 1025 °C.[47] The observed increase in grain size between 1000 °C and 1200 °C is likely caused by the presence of this liquid phase.

Besides, within the cement phase, the Lithium oxide and the yttria can also react. Using a similar sol-gel method to prepare $LiYO_2$, Loembe et *al* reported that the crystallization of $LiYO_2$ occurs at 950 °C with an excess of Li (Li:Y=3:1).[48] Even higher temperature was reported to be necessary for a lower Li/Y molar ratio which explains why no crystallized $LiYO_2$ phase can be observed above 1000 °C in the XRD pattern. However, the formation of the $LiYO_2$ can be confirmed by the FTIR, see Fig. 11 The first absorption at 865 cm^{-1} is consistent with Y–O octahedron vibration modes. The peaks located at 1437-1500 cm^{-1} are assigned to Y–O/Li bending mode. It can be observed that the $LiYO_2$ was formed at 400 °C. Between 600 °C and 800 °C, the peak intensity reduced significantly. For a temperature higher than 1000 °C, the peaks disappeared.

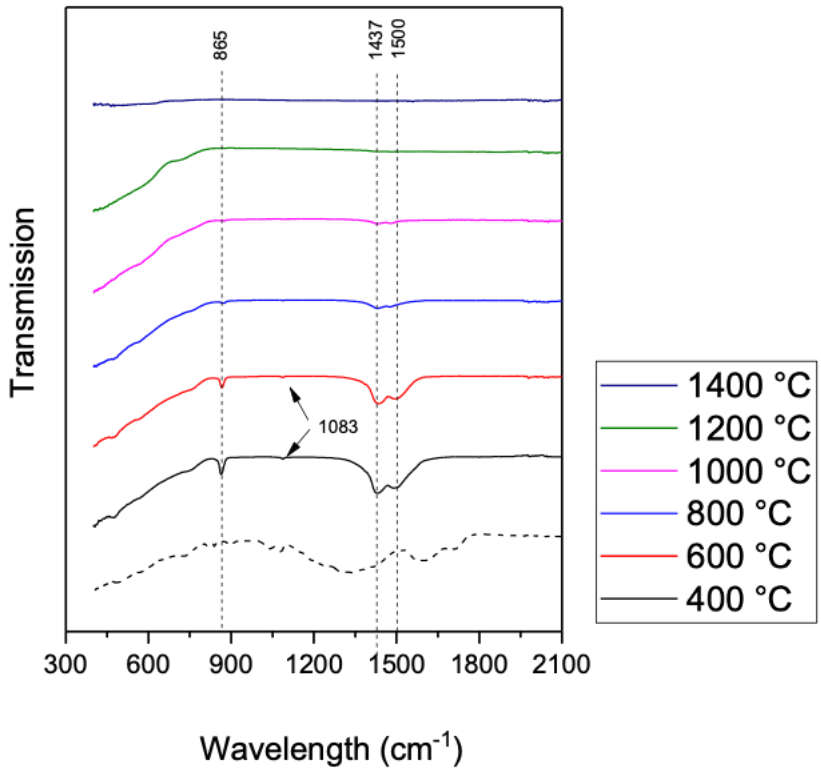

Fig. 11: the FTIR of the pellets as a function of the sintering temperature.

It is now possible to trace the evolution of the microstructure and the phases transition in the ternary (Li,Y,Zr) oxide system as a function of the sintering temperature, see Fig. 12. At 400 °C and 600 °C, the mixture was composed of monoclinic and tetragonal 3YSZ and the oxide derived from solution. Then the Li_2ZrO_3 was formed at a temperature between 600 °C and 800 °C while the $LiYO_2$ was formed at around 700 °C. For a temperature between 800 and 1000 °C, the transition consisted mainly of a monoclinic to tetragonal transition of YSZ. For a temperature higher than 1000 °C (1045 °C) the formation of the cubic phase predominated with the yttria diffusion into zirconia. From 1000 °C to 1200 °C, a liquid phase can be formed according to the Li_2O-ZrO_2 phase diagram.[47] As consequence, a grain coarsening is observed of the pellet which is accompanied by a densification. Thus, obtaining a dense fine final miscrostructure avoiding grain coarsening needs an accurate controle of temperature just above 1000 °C.

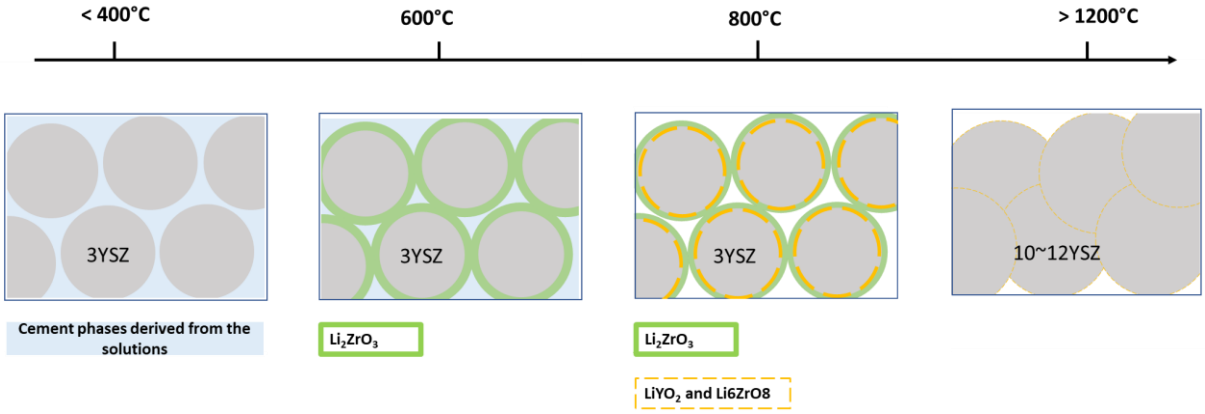

Fig. 12: the phase evolution during sintering process of Li_2Y-pH2

4. Conclusion

This study highlights the significant potential of a modified wet-chemical methods for the preparation of YSZ materials. The strength of the technique lies mainly in its high homogeneity and versatility enabling the control over ceramic microstructure. Additionally, it exhibits substantial scalability potential, addressing longstanding challenges in industry, particularly related to the optimization complexity and the energy efficiency of conventional ways. By simply adjusting the citric acid content (pH of solution), this method streamlines the optimization process by effectively controlling the cement's composition. Notably, two pH ranges have been identified as potentially interesting: a low pH stage ($pH \leqslant 2$) where a dense structure can be achieved, and a slightly higher pH stage ($pH \approx 3$) where a porous structure is formed through a combustion mechanism, offering versatility in tailoring YSZ properties to diverse application requirements. Reducing sintering temperatures through lithium doping holds special importance amid today's energy crises. The effect of Lithium dopant has also been evidenced. The sample with a molar ratio Li/ Y equaling to 2 allows a significant enhanced densification compared with the sample have lower Lithium content. Nevertheless, further investigation of the process is necessary, including the exploration of the influence of yttria content and the sintering process on the final product density and phases composition. Our ongoing research aims, at first, to strike the ideal equilibrium between solution composition and homogeneity, enabling the attainment of a suitable physicochemical and mechanical properties in ceramic products. Subsequently, the perspective study will explore the impact of Li dopant in the electronic domain, particularly for high-temperature applications.

Reference

[1] J.R. Kelly, I. Denry, Stabilized zirconia as a structural ceramic: An overview, Dent. Mater. 24 (2008) 289–298. https://doi.org/10.1016/J.DENTAL.2007.05.005.

[2] K. Matsui, H. Yoshida, Y. Ikuhara, Review: microstructure-development mechanism during sintering in polycrystalline zirconia, Https://Doi.Org/10.1080/09506608.2017.1402424. 63 (2017) 375–406. https://doi.org/10.1080/09506608.2017.1402424.

[3] C. Piconi, G. Maccauro, Zirconia as a ceramic biomaterial, Biomaterials. 20 (1999) 1–25. https://doi.org/10.1016/S0142-9612(98)00010-6.

[4] Z.Y. Wei, G.H. Meng, L. Chen, G.R. Li, M.J. Liu, W.X. Zhang, L.N. Zhao, Q. Zhang, X.D. Zhang, C.L. Wan, Z.X. Qu, L. Chen, J. Feng, L. Liu, H. Dong, Z. Bin Bao, X.F. Zhao, X.F. Zhang, L. Guo, L. Wang, B. Cheng, W.W. Zhang, P.Y. Xu, G.J. Yang, H.N. Cai, H. Cui, Y. Wang, F.X. Ye, Z. Ma, W. Pan, M. Liu, K.S. Zhou, C.J. Li, Progress in ceramic materials and structure design toward advanced thermal barrier coatings, J. Adv. Ceram. 2022 117. 11 (2022) 985–1068. https://doi.org/10.1007/S40145-022-0581-7.

[5] Z. Zakaria, S.H. Abu Hassan, N. Shaari, A.Z. Yahaya, Y. Boon Kar, A review on recent status and challenges of yttria stabilized zirconia modification to lowering the temperature of solid oxide fuel cells operation, Int. J. Energy Res. 44 (2020) 631–650. https://doi.org/10.1002/ER.4944.

[6] O.E. Oskouyi, A. Maghsoudipour, M. Shahmiri, M. Hasheminiasari, Preparation of YSZ electrolyte coating on conducting porous Ni–YSZ cermet by DC and pulsed constant voltage electrophoretic deposition process for SOFCs applications, J. Alloys Compd. 795 (2019) 361–369. https://doi.org/10.1016/J.JALLCOM.2019.04.334.

[7] D. Chen, C. Dambra, M. Dorfman, Process and properties of dense and porous vertically-cracked yttria stabilized zirconia thermal barrier coatings, Surf. Coatings Technol. 404 (2020) 126467. https://doi.org/10.1016/J.SURFCOAT.2020.126467.

[8] C. Viazzi, J.P. Bonino, F. Ansart, Synthesis by sol-gel route and characterization of Yttria Stabilized Zirconia coatings for thermal barrier applications, Surf. Coatings Technol. 201 (2006) 3889–3893. https://doi.org/10.1016/J.SURFCOAT.2006.07.241.

[9] J.A. Lee, H.C. Lee, Y.W. Heo, J.H. Lee, J.J. Kim, Effect of Li doping on sintering characteristics and microstructural behavior of yttria-stabilized zirconia, Ceram. Int. 42 (2016) 17339–17346.

https://doi.org/10.1016/J.CERAMINT.2016.08.030.

[10] A. Cordier, H. El Khal, E. Siebert, M.C. Steil, On the role of the pore morphology on the electrical conductivity of porous yttria-stabilized zirconia, J. Eur. Ceram. Soc. 39 (2019) 2518–2525. https://doi.org/10.1016/J.JEURCERAMSOC.2019.02.027.

[11] R. Liu, C.A. Wang, Effects of mono-dispersed PMMA micro-balls as pore-forming agent on the properties of porous YSZ ceramics, J. Eur. Ceram. Soc. 33 (2013) 1859–1865. https://doi.org/10.1016/J.JEURCERAMSOC.2013.01.036.

[12] G.S. Lewis, A. Atkinson, B.C.H. Steele, Cobalt additive for lowering the sintering temperature of yttria-stabilized zirconia, J. Mater. Sci. Lett. 20 (2001) 1155–1157. https://doi.org/10.1023/A:1010912912157/METRICS.

[13] Y. Lim, H. Lee, J. Park, Y.B. Kim, Low-temperature constrained sintering of YSZ electrolyte with Bi2O3 sintering sacrificial layer for anode-supported solid oxide fuel cells, Ceram. Int. 48 (2022) 9673–9680. https://doi.org/10.1016/J.CERAMINT.2021.12.168.

[14] E. Bakan, R. Vaßen, Ceramic Top Coats of Plasma-Sprayed Thermal Barrier Coatings: Materials, Processes, and Properties, J. Therm. Spray Technol. 2017 266. 26 (2017) 992–1010. https://doi.org/10.1007/S11666-017-0597-7.

[15] D.E. Wolfe, J. Singh, R.A. Miller, J.I. Eldridge, D.M. Zhu, Tailored microstructure of EB-PVD 8YSZ thermal barrier coatings with low thermal conductivity and high thermal reflectivity for turbine applications, Surf. Coatings Technol. 190 (2005) 132–149. https://doi.org/10.1016/J.SURFCOAT.2004.04.071.

[16] C.A. da Silva, N.F.P. Ribeiro, M.M.V.M. Souza, Effect of the fuel type on the synthesis of yttria stabilized zirconia by combustion method, Ceram. Int. 35 (2009) 3441–3446. https://doi.org/10.1016/J.CERAMINT.2009.06.005.

[17] Z. Huang, W. Han, Z. Feng, J. Qi, D. Wu, N. Wei, Z. Tang, Y. Zhang, J. Duan, T. Lu, The effects of precipitants on co-precipitation synthesis of yttria-stabilized zirconia nanocrystalline powders, J. Sol-Gel Sci. Technol. 90 (2019) 359–368. https://doi.org/10.1007/S10971-019-04947-Y/FIGURES/9.

[18] R.M. Smith, X.D. Zhou, W. Huebner, H.U. Anderson, Novel yttrium-stabilized zirconia polymeric precursor for the fabrication of thin films, J. Mater. Res. 19 (2004) 2708–2713. https://doi.org/10.1557/JMR.2004.0352/METRICS.

[19] T. Razpotnik, M. Marinšek, B. Novosel, K. Zupan, V. Francetič, J. Maček, A polymer complex solution process for the synthesis and characterization of Ni–YSZ cermet material, Ceram. Int. 34 (2008) 1741–1746. https://doi.org/10.1016/J.CERAMINT.2007.05.006.

[20] T. Okubo, H. Nagamoto, Low-temperature preparation of nanostructured zirconia and YSZ by sol-gel processing, J. Mater. Sci. 30 (1995) 749–757. https://doi.org/10.1007/BF00356338/METRICS.

[21] Z. Shao, W. Zhou, Z. Zhu, Advanced synthesis of materials for intermediate-temperature solid oxide fuel cells, Prog. Mater. Sci. 57 (2012) 804–874. https://doi.org/10.1016/J.PMATSCI.2011.08.002.

[22] E.A. Cochran, D.H. Park, M.G. Kast, L.J. Enman, C.K. Perkins, R.H. Mansergh, D.A. Keszler, D.W. Johnson, S.W. Boettcher, Role of Combustion Chemistry in Low-Temperature Deposition of Metal Oxide Thin Films from Solution, Chem. Mater. 29 (2017) 9480–9488. https://doi.org/10.1021/ACS.CHEMMATER.7B03618/SUPPL_FILE/CM7B03618_SI_001.PDF.

[23] A.J. Flegler, T.E. Burye, Q. Yang, J.D. Nicholas, Cubic yttria stabilized zirconia sintering additive impacts: A comparative study, Ceram. Int. 40 (2014) 16323–16335. https://doi.org/10.1016/J.CERAMINT.2014.07.071.

[24] N. Osman, A. Abdul Samat, A.N. Che Mat, N.I. Abd Malek, J. Andas, Chelating agent size effect on thermal decomposition, phase formation and morphology characteristics of Y3+ doped Ba(Ce,Zr)O3

ceramics powder prepared by a sol-gel process, Ceram. Int. 48 (2022) 2289–2297. https://doi.org/10.1016/J.CERAMINT.2021.10.007.

[25] J.A. Krogstad, M. Lepple, Y. Gao, D.M. Lipkin, C.G. Levi, Effect of Yttria Content on the Zirconia Unit Cell Parameters, J. Am. Ceram. Soc. 94 (2011) 4548–4555. https://doi.org/10.1111/J.1551-2916.2011.04862.X.

[26] E.A. Cochran, K.N. Woods, D.W. Johnson, C.J. Page, S.W. Boettcher, Unique chemistries of metal-nitrate precursors to form metal-oxide thin films from solution: materials for electronic and energy applications, J. Mater. Chem. A. 7 (2019) 24124–24149. https://doi.org/10.1039/C9TA07727H.

[27] J. Farjas, J. Camps, P. Roura, S. Ricart, T. Puig, X. Obradors, Thermoanalytical study of the formation mechanism of yttria from yttrium acetate, Thermochim. Acta. 521 (2011) 84–89. https://doi.org/10.1016/J.TCA.2011.04.009.

[28] M. Ibrahim, A. Nada, & Diaa, E. Kamal, Density functional theory and FTIR spectroscopic study of carboxyl group, IJPAP Vol.43(12) [December 2005]. 43 (2005) 911–917. http://nopr.niscpr.res.in/handle/123456789/8906 (accessed June 28, 2023).

[29] M.K. Trivedi, A. Branton, D. Trivedi, G. Nayak, K. Bairwa, S. Jana, Spectroscopic Characterization of Disodium Hydrogen Orthophosphate and Sodium Nitrate after Biofield Treatment, J. Chromatogr. Sep. Tech. 6 (2015) 1–5. https://doi.org/10.4172/2157-7064.1000282.

[30] A. Mali, A. Ataie, Structural characterization of nano-crystalline BaFe12O19 powders synthesized by sol–gel combustion route, Scr. Mater. 53 (2005) 1065–1070. https://doi.org/10.1016/J.SCRIPTAMAT.2005.06.037.

[31] M. Huang, K. Guo, Z. Man, H. Chen, X. Yang, F. Xu, J. Zhao, Morphology controllable synthesis of yttrium oxide-based phosphors from yttrium citrate precursors, J. Rare Earths. 29 (2011) 830–836. https://doi.org/10.1016/S1002-0721(10)60551-0.

[32] M.E. Miller, L.P. McKinnon, E.B. Walker, Quantitative measurement of metal chelation by fourier transform infrared spectroscopy, Anal. Chem. Res. 6 (2015) 32–35. https://doi.org/10.1016/J.ANCR.2015.10.002.

[33] W. Janusz, E. Skwarek, D. Sternik, S. Pikus, Synthesis and thermogravimetric analysis of monoclinic yttrium citrate dihydrate, J. Therm. Anal. Calorim. 146 (2021) 1027–1038. https://doi.org/10.1007/S10973-020-10107-0/FIGURES/10.

[34] A. Massoud, H.E. Rizk, M.F. Attallah, Selective separation of Y(III) from Sr(II) using hybrid polymer: synthesis, characterization, batch and column study, Polym. Bull. 2020 7812. 78 (2020) 7053–7069. https://doi.org/10.1007/S00289-020-03479-8.

[35] W. Janusz, E. Skwarek, D. Sternik, S. Pikus, D. Pawlak, J.L. Parus, R. Mikołajczak, Synthesis of yttrium citrate from yttrium carbonate hydroxide and citric acid, Mater. Chem. Phys. 250 (2020) 123113. https://doi.org/10.1016/J.MATCHEMPHYS.2020.123113.

[36] W. Janusz, E. Skwarek, D. Sternik, Preparation of yttrium citrate by the reaction of yttrium hydroxide with sodium citrate, Physicochem. Probl. Miner. Process. 56 (2020) 51–59. https://doi.org/10.37190/PPMP/126682.

[37] S.S. Balabanov, E.M. Gavrishchuk, D.A. Permin, Synthesis and properties of yttrium hydroxyacetate sols, Inorg. Mater. 2012 485. 48 (2012) 500–503. https://doi.org/10.1134/S0020168512050020.

[38] M. Hajizadeh-Oghaz, R.S. Razavi, M. Barekat, M. Naderi, S. Malekzadeh, M. Rezazadeh, Synthesis and characterization of Y2O3 nanoparticles by sol–gel process for transparent ceramics applications, J. Sol-Gel Sci. Technol. 2016 783. 78 (2016) 682–691. https://doi.org/10.1007/S10971-016-3986-3.

[39] The Synthesis of Single Tetragonal Phase Zirconia by SolGel Route - UCL Discovery, (n.d.). https://discovery.ucl.ac.uk/id/eprint/1533032/ (accessed July 2, 2022).

[40] Z. Haghi, S.M. Masoudpanah, CTAB-assisted solution combustion synthesis of LiFePO4 powders, J. Sol-Gel Sci. Technol. 2019 912. 91 (2019) 335–341. https://doi.org/10.1007/S10971-019-05002-6.

[41] S. Famenin Nezhad Hamedani, S.M. Masoudpanah, M.S. Bafghi, N. Asgharinezhad Baloochi, Solution combustion synthesis of CoFe2O4 powders using mixture of CTAB and glycine fuels, J. Sol-Gel Sci. Technol. 2018 863. 86 (2018) 743–750. https://doi.org/10.1007/S10971-018-4671-5.

[42] K. Tõnsuaadu, A. Zalga, A. Beganskiene, A. Kareiva, Thermoanalytical study of the YSZ precursors prepared by aqueous sol–gel synthesis route, J. Therm. Anal. Calorim. 2012 1101. 110 (2012) 77–83. https://doi.org/10.1007/S10973-011-2184-3.

[43] K. Tõnsuaadu, A. Zalga, A. Beganskiene, A. Kareiva, Thermoanalytical study of the YSZ precursors prepared by aqueous sol-gel synthesis route, J. Therm. Anal. Calorim. 110 (2012) 77–83. https://doi.org/10.1007/S10973-011-2184-3.

[44] D.F. Zambrano, A. Barrios, L.E. Tobón, C. Serna, P. Gómez, J.D. Osorio, A. Toro, Thermal properties and phase stability of Yttria-Stabilized Zirconia (YSZ) coating deposited by Air Plasma Spray onto a Ni-base superalloy, Ceram. Int. 44 (2018) 3625–3635. https://doi.org/10.1016/J.CERAMINT.2017.11.109.

[45] Y. Zou, Structure and Properties of Lithium Ion Conductors in the Li2O-Y2O3-ZrO2 System, (1993). https://canadaresearch.mcmaster.ca/handle/11375/19215 (accessed July 13, 2023).

[46] K. Yuan, X. Jin, C. Xu, X. Wang, G. Zhang, L. Zhu, D. Xu, Fabrication of dense and porous Li2ZrO3 nanofibers with electrospinning method, Appl. Phys. A Mater. Sci. Process. 124 (2018) 1–10. https://doi.org/10.1007/S00339-018-1821-0/METRICS.

[47] G.P. Wyers, E.H.P. Cordfunke, Phase relations in the system Li2O-ZrO2, J. Nucl. Mater. 168 (1989) 24–30. https://doi.org/10.1016/0022-3115(89)90560-6.

[48] H.W. L.M Loembe, Z.Y. Fu, W.M. Wang, Sol-Gel Synthesis and Characterization of Lithium Yttrium Oxide, Int. J. Res. Eng. Technol. 04 (2015) 1–7. https://doi.org/10.15623/ijret.2015.0406001.